*Supporting Information*

**Strong Purcell Enhancement at Telecom Wavelengths Afforded by Spinel Fe$_3$O$_4$ Nanocrystals with Size-Tunable Plasmonic Properties**

Ekaterina A. Dolgopolova,[a] Dongfang Li,[a] Steven T. Hartman,[b] John Watt,[a] Carlos Ríos,[c,d] Juejun Hu,[c] Ravi Kukkadapu,[e] Joanna Casson,[f] Riya Bose,[g] Anton V. Malko,[g] Anastasia V. Blake,[a] Sergei Ivanov,[a] Oleksiy Roslyak[h], Andrei Piryatinski,[i] Han Htoon,[a] Hou-Tong Chen,[a] Ghanshyam Pilania,[b] Jennifer A. Hollingsworth[a*]

[a.] Materials Physics and Applications Division: Center for Integrated Nanotechnologies, Los Alamos National Laboratory, Los Alamos, NM 87545, United States
[b.] Materials Science & Technology Division, Los Alamos National Laboratory, Los Alamos, NM 87545, United States
[c.] Department of Materials Science & Engineering, Massachusetts Institute of Technology, Cambridge, MA 02139, United States
[d.] Institute for Research in Electronics and Applied Physics, University of Maryland, College Park, MD 20742, USA
[e.] Environmental Molecular Sciences Laboratory, Pacific Northwest National Laboratory, Richland, WA 99354, United States
[f.] Chemistry Division, Los Alamos National Laboratory, Los Alamos, NM 87545, United States
[g.] Department of Physics, The University of Texas at Dallas, Richardson, TX 75080, United States
[h.] Department of Physics and Engineering Physics, Fordham University, Bronx, NY 10458, United States
[i.] Theoretical Division, Los Alamos National Laboratory, Los Alamos, NM 87545, United States

**Table of contents:**

**Materials.** Iron(II) acetylacetonate (97%, Combi-Blocks), iron(III) acetylacetonate (99.9%, Sigma-Aldrich), lead(II) chloride (99.999%, Alfa Aesar), cadmium oxide (>99.99%, Sigma-Aldrich, oleylamine (technical grade, 70%, Sigma-Aldrich), oleic acid (90%, Alfa Aesar), benzyl ether (99%, Acros Organic), octadecene (technical grade, 90%, Sigma-Aldrich), 1,2-hexadecanodiol (90%, Sigma-Aldrich), sulfur (99.999%, Acros Organics), chloroform (≥99.8%, Sigma-Aldrich), ethanol (200 proof, Electron Microscopy Sciences), 1-butanol (99.9%, Sigma-Aldrich), carbon disulfide (ACS grade, Sigma-Aldrich), carbon tetrachloride (reagent grade, 99.9%, Sigma-Aldrich), tetrachloroethylene (99.5%, Sigma-Aldrich), and methanol (>99.9%, Sigma-Aldrich) were used as received without any further purification. All syntheses were carried out under an argon atmosphere using standard Schlenk line techniques. PbS/CdS QDs were prepared according to previously reported literature procedure.[1]

**Preparation of $Fe_3O_4$ NPs.**
**Approach I.** The samples were prepared by adaptation of the literature procedure.[2] In a 50 mL round-bottom flask, 0.5 mmol of $Fe(acac)_3$ (0.18 g) (**A-I-1**) or $Fe(acac)_2$ (0.13 g) (**A-I-2**) were evacuated for 20 min under vacuum at room temperature. Then, a mixture of oleic acid (1.5 mmol, 0.47 mL), oleylamine (1.5 mmol, 0.49 mL), 1,2-hexadecanediol (2.5 mmol, 0.295 g), and benzyl ether (5 mL) was added to the flask. The resulting reaction mixture was heated to 200 °C at the rate of 20 °/min and allowed to anneal for 24 h. After 24 h, the reaction mixture was cooled down to room temperature. The obtained dark brown nanoparticles were washed three times by dispersion in chloroform, followed by precipitation by addition of ethanol.
**Approach II.** The sample was prepared by adaptation of the literature procedure.[3] The variation in the reaction time was used to achieve a control over nanoparticle size. In a 50 mL round-bottom flask, $Fe(acac)_3$ (0.14 g, 0.40 mmol) was added to a mixture of oleic acid (0.25 ml) and benzyl ether (3.9 ml). The resulting mixture was degassed for 1 h at room temperature. Then, the solution was heated to 290 °C at the rate of 20 °/min. The reaction mixture was kept at this temperature for 0.5 or 1 h and then cooled down to room temperature. The resulting dark brown nanoparticles were washed three times by dispersion in chloroform, followed by precipitation by addition of ethanol.
**Approach III.** The samples were prepared using modified literature procedure.[4] The effect of precursor nature and reaction temperature was investigated. In a typical synthesis, 0.34 g $Fe(acac)_3$ (0.96 mmol) or 0.25 mg $Fe(acac)_2$ (0.96 mmol) were dissolved in a mixture of 1.0 mL oleylamine, 2.2 mL oleic acid, and 6.1 mL octadecene in a 50 mL round bottom three-neck flask. The resulting mixture was heated to 80 °C to dissolve all the materials. The solution was then degassed at 130 °C for 1 h and heated to the reaction temperature (Table S1) under argon flux for 1 h. After 1 h, the reaction mixture was cooled down to room temperature. The obtained dark brown nanoparticles were washed three times by dispersion on chloroform, followed by precipitation by addition of ethanol.

**Nanocrystal Characterization.** Nanocrystal size and shape were assessed by transmission electron microscopy (TEM) using a JOEL 2010 operating at 200 kV. The average diameter and standard deviation in sizes of different NCs were obtained by analyzing 200 NCs from their corresponding TEM images using ImageJ software and fitting the statistics to a Gaussian size distribution. Absorption spectra were collected on a Cary Varian 5000 UV-Vis-NIR spectrophotometer. Emission spectra were collected using a Horiba Scientific Nanolog spectrofluorimeter using a 450 W Xe arc lamp for excitation. Mössbauer spectroscopy measurements were collected with a WissEl Elektronik (Germany) instrument that included a

closed-cycle cryostat SHI-850 unit obtained from Janis Research Company, Inc., (Wilmington, MA), a Sumitomo CKW-21 He compressor unit (Allentown, PA), and a <75 mCi [57]Co/Rh source (See Co, Edina, MN). An Ar-Kr proportional counter obtained from LND Inc. (Oceanside, NY) was used as the detector. The setup data was folded to provide a flat background and a zero-velocity position corresponding to the center shift (CS) of a metal Fe foil (7-mm) at room temperature. Data was collected slightly above the Verwey transition temperature of the magnetite (120-140 K) to estimate Fe(II)/Fe(III) ratio of the solids.[5] The data was modeled with Recoil software (University of Ottawa, Canada) using a Voigt-based structural fitting routine, as outlined by Rancourt and Ping.[6] The sample preparation (type of the sample holder, etc.) was similar to the procedure reported in Boiteau *et al.,* 2019.[7] DC magnetization curves were recorded from -2.38 x $10^6$ A/m to 2.38 x $10^6$ A/m at 50 K using a Quantum Designs Versalab vibrating sample magnetometer (VSM).
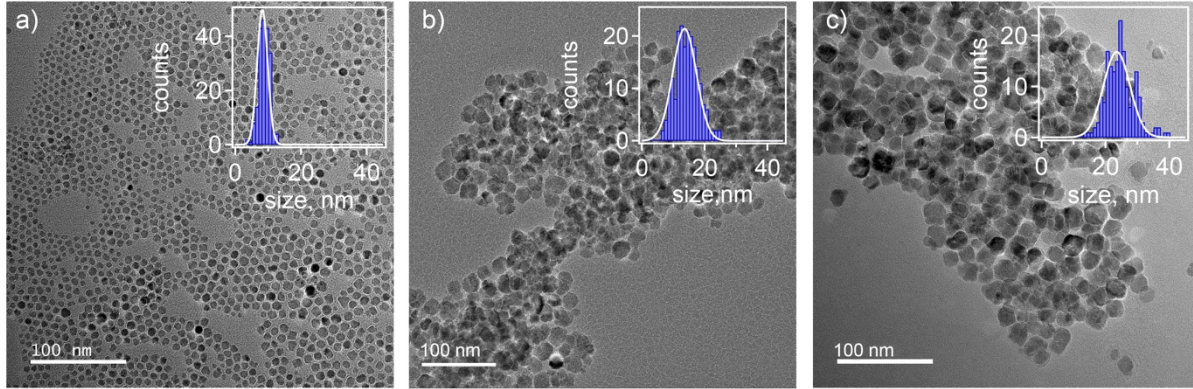
**Figure S1.** Representative TEM images and respective size distribution histograms of Fe$_3$O$_4$ NCs with different particle sizes a) 8.2 ± 1.6 nm; b) 13.6 ± 3.7 nm, and c) 20.7 ± 4.5 nm.

**Table S1.** Synthetic parameters, NC diameter, calculated maghemite shell thickness, $\lambda_{max}$ and $E_g$ for the obtained NCs.

| | time, h | t, °C | D$_{TEM}$, nm | e, nm | $\lambda_{max}$, nm | $E_g$, eV |
|---|---|---|---|---|---|---|
| **Approach I** | | | | | | |
| **A-I-1** | 24 | 200 | 5.2±1.1 | 0.67 | 1287 | 1.04 |
| **A-I-2** | | 200 | 6.3±1.8 | 0.50 | 1383 | 1.25 |
| **Approach II** | | | | | | |
| **A-II-1** | 0.5 | 290 | 18.2±4.3 | 1.2 | 1491 | 0.90 |
| **A-II-2** | | 290 | 13.6±3.7 | | 1444 | 1.09 |
| **A-II-3** | 1 | 290 | 23.5±3.6 | 0.4 | 1738 | 0.76 |
| **A-II-4** | | 290 | 20.7±4.5 | | 1693 | 0.81 |
| **Approach III** | | | | | | |
| **A-III-1** | | 310 | 9.2±2.5 | 0.48 | 1458 | 1.04 |
| **A-III-2** | | 310 | 9.5±2.0 | | 1394 | 1.25 |
| **A-III-3** | | 310 | 8.2±1.6 | 0.56 | 1437 | 1.14 |
| **A-III-4** | 1 | 260 | 7.3±4.0 | 0.50 | 1382 | 1.06 |
| **A-III-5** | | 280 | 8.5±2.5 | 0.54 | 1319 | 1.18 |
| **A-III-6** | | 290 | 16.0±3.0 | | 1602 | 0.85 |
| **A-III-7** | | 300 | 8.1±3.5 | 0.33 | 1418 | 1.30 |

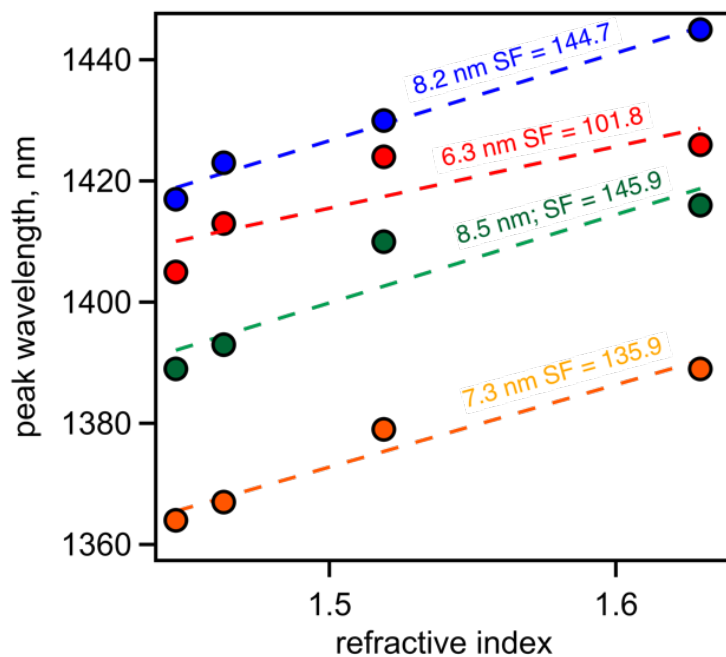**Figure S2.** LSPR peak wavelength plotted as a function of the solvent refractive index for $Fe_3O_4$ NCs: **A-III-4** (orange), **A-III-5** (green), **A-I-2** (red), and **A-III-3** (blue). The dashed lines show liner fits.
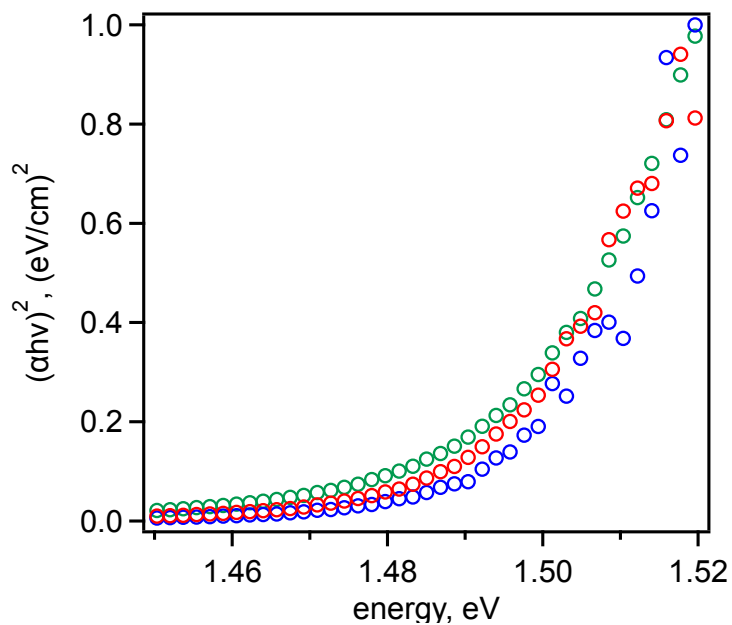


**Figure S3.** Plots of $(\alpha h\nu)^2$ vs photon energy for **A-III-4** in different solvents: chloroform (red), trichloroethylene (green), and carbon disulfide (blue).

**Technical details of DFT computations:**

To compute the electronic band structure of bulk magnetite, DFT computations were performed using the projector augmented wave (PAW) method as implemented within the Vienna *Ab Initio* Simulation Package (VASP). Generalized gradient approximation (GGA) of Perdew, Burke and Ernzerhof (PBE) for the exchange–correlation potential, a 500 eV cut-off energy for the plane wave basis set and a $10^{-5}$ eV energy convergence criterion for the self-consistent field cycles of the electronic charge density were employed. A Gamma-centered $3 \times 3 \times 3$ *k*-point mesh was used for the Brillouin zone sampling and a Hubbard correction with U = 5.3 eV within the Dudarev's formulation was required to correctly describe the localized *d*-orbitals of Fe. Spin polarized calculations were performed with all the magnetic moments on Fe atoms ferromagnetically aligned within each of the $O_h$ and $T_d$ sites, while antiferromagnetically aligned with respect to each other.

Supercells containing 16 Fe atoms at the octahedral sublattice and 8 tetrahedrally coordinated Fe atoms were considered to model the inverse $Fe_3O_4$ spinel structure within the low temperature tetragonal $P4_122$ and high temperature cubic Fd-3m phases. Our computations show that a symmetry breaking going from the cubic to the tetragonal phase leads to a slight lowering of the total energy (0.11 eV/formula unit) with slight opening of the bandgap. For the subsequent computations, the low energy configuration was considered.

For the stochiometric case, all the Fe atoms at the $T_d$ sites exhibit a +3 oxidation state, while an equimolar ordered ground state configuration of $Fe^{3+}$ and $Fe^{2+}$ ions is adopted at the $O_h$ sites. Nonstoichiometric magnetite bulk structures were simulated either by adding or removing one or two electrons per supercell. The added (removed) electrons lead to a higher (lower) ratio of $Fe^{2+}/Fe^{3+}$ on the octahedral sublattice. For the nonstoichiometric cases involving either added or removed electrons, first-order monopole corrections were used to adequately correct for unphysical electrostatic interactions of the charged finite supercells with periodic boundary conditions. The geometry of the bulk stoichiometric system was fully relaxed by allowing the volume, cell shape and the internal coordinates to change during the relaxation process and the lattice parameter of the cubic cell was kept fixed at the optimized value of 8.537 Å for subsequent nonstoichiometric computations with either one or two electrons added or removed. Density functional perturbation theory was used to compute the electronic contribution of the dielectric permittivity.

Defect formation energies in $Fe_3O_4$ were calculated using a 112-atom *$P4_122$* supercell, with finite-size corrections according to the method of Freysoldt *et al*. for charged defects.[8] Defect structures were generated using the PyCDT software package[9] and calculated in compatibility with the PBE + U calculations of the Materials Project, which required adding the metal oxide correction that is used in the Materials Project but not currently implemented in PyCDT. We also applied band edge shifting corrections for an HSE06 band gap of 0.65 eV, and band filling corrections, and plotted the results using Pymatgen.

The defect computations identify Fe vacancy on the octahedral site as a point defect with particularly low defect formation energy. For instance, the neutral Fe octahedral vacancy formation energy was computed to be -19 meV for the $Fe_2O_3/Fe_3O_4$ equilibrium chemical potentials. This result implies that stoichiometric $Fe_3O_4$ is close to the convex hull but not exactly on the convex hull (at least at the level of the theory used in these defects computations). But we also note that the computed defect formation energy is very low and falls within the error bars of these defect computations (for instance, the Materials Project's tests indicate that the standard error when comparing corrected PBE + U formation energies of metal oxides is 24 meV). Nevertheless, our computations clearly indicate that the formation of Fe vacancies on the octahedral sublattice

is thermodynamically highly favored. This is in agreement with our experimental observations as well as past studies reported in the literature. For example, a number of studies focused on studying the high-temperature equilibria of $Fe_3O_4$, $Fe_2O_3$ and oxygen indicate that at fixed oxygen pressure the iron deficiency in $Fe_3O_4$ is increases as temperature is lowered.[10, 11] Furthermore, for the iron-deficient magnetite, $Fe^{3+}[Fe^{3+}_{1+2x} Fe^{2+}_{1-3x}]O^{2-}_4$ (where x is the number of iron vacancies per $Fe_3O_4$ in the spinel structure), there are metastable natural occurrences of all compositions up to $x = 1/3$.[12, 13]
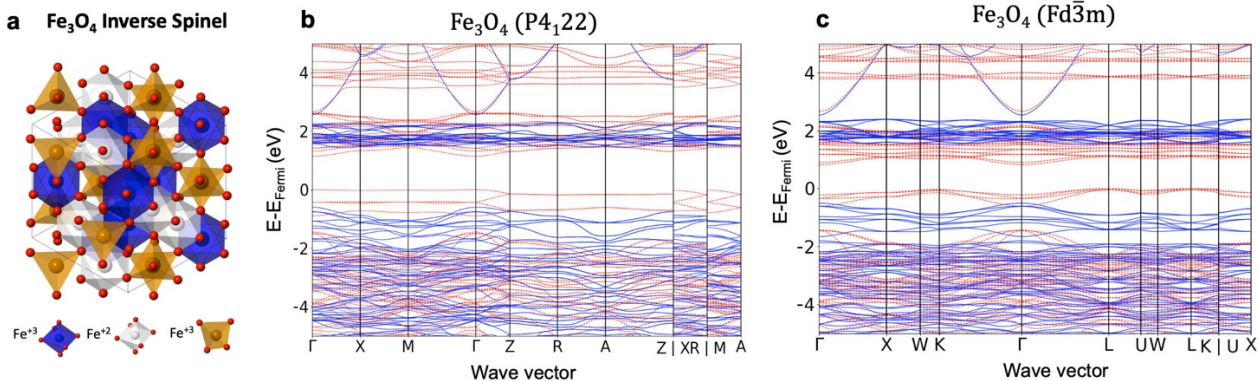
**Figure S4.** (*a*) Fe$_3$O$_4$ inverse spinel structure. (*b, c*) DFT-computed electronic band structures of Fe$_3$O$_4$. Spin up and spin down channels are shown in blue and red, respectively.
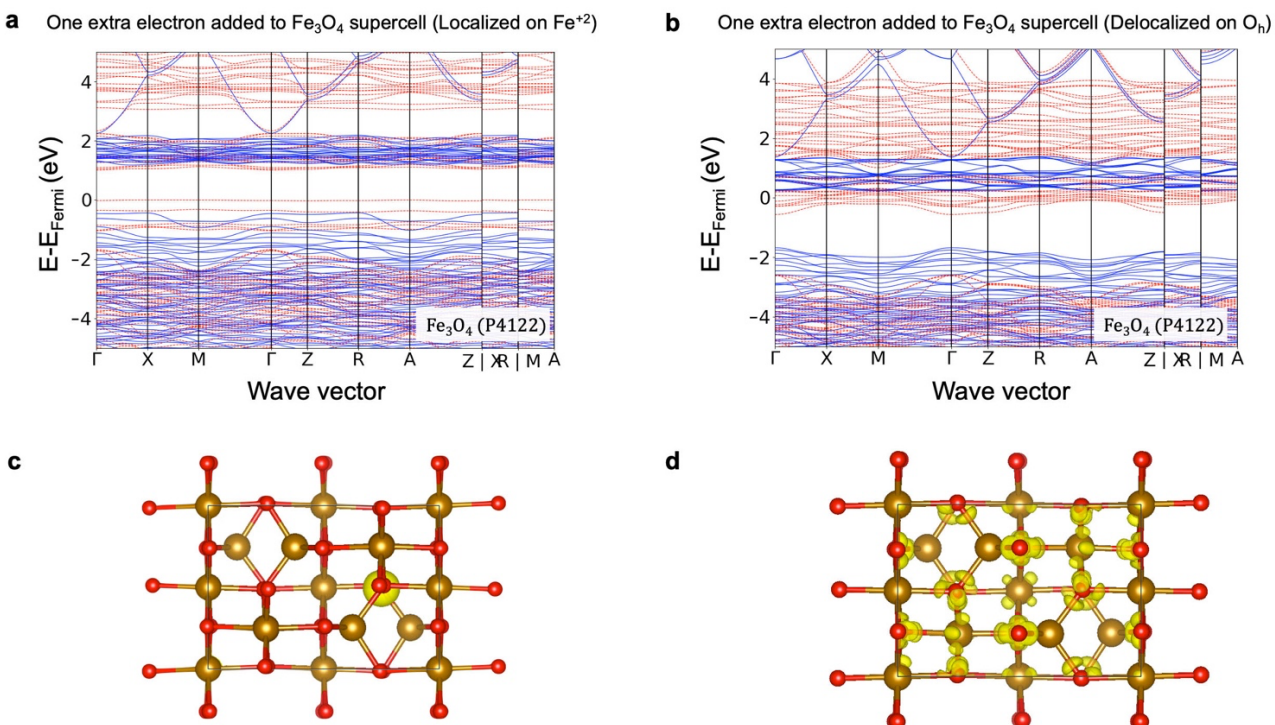


**Figure S5.** DFT-computed electronic band structure for Fe$_3$O$_4$ when one electron is added to the supercell. The added electron can either localize on one of the Fe$^{+3}$ cations reducing it to a +2-oxidation state (*a*) or delocalize via the traditional n-type doping behavior, creating filled states near the conduction band edge (*b*). In each case, the spin up and spin down channels are shown in blue and red, respectively. (*c*) and (*d*) visualize the charge density associated with the bands created by the added electrons corresponding to the (*a*) and (*b*) panels, respectively.
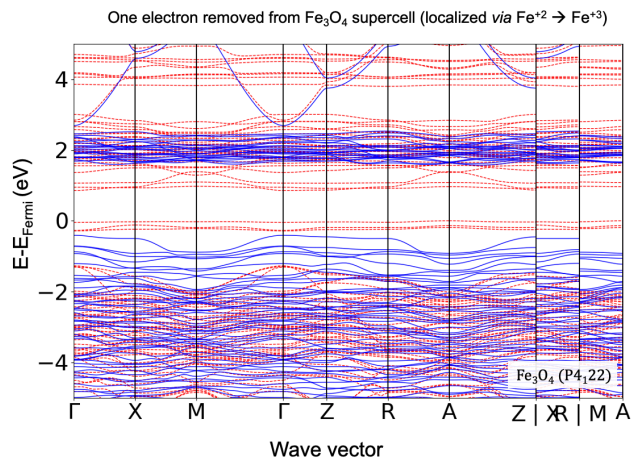
**Figure S6.** DFT-computed electronic band structure of off stoichiometric $Fe_3O_4$ with one electron removed from the supercell. Spin up and spin down channels are shown in blue and red, respectively. As a result of the electron removal, one $Fe^{+2}$ cation on the octahedral sublattice is oxidized to a +3-oxidation state leading to the disappearance of a band near the Fermi energy as compared to the stoichiometric case.
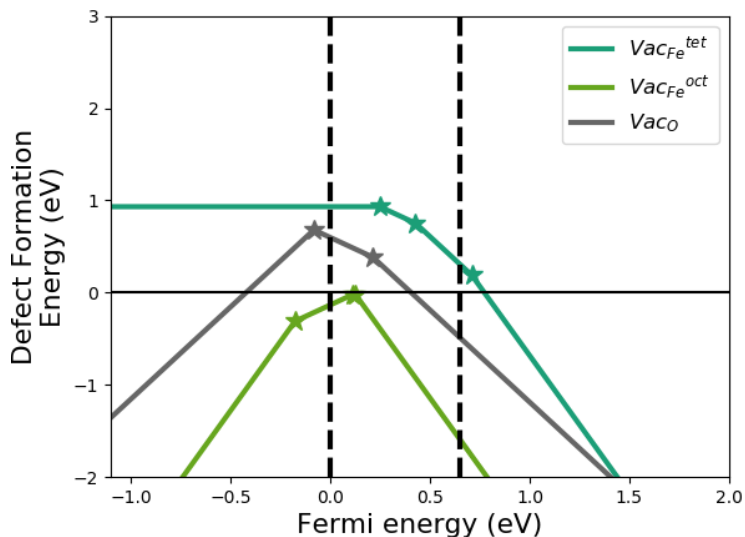


**Figure S7.** The computed formation energies of point defects in $Fe_3O_4$, with the chemical potentials defined by the equilibrium with $Fe_2O_3$ (oxygen-rich conditions).

**Calculation of magnetic dead layer.** Assuming that each nanoparticle consists of magnetite core having a magnetic structure and magnetically disordered maghemite shell, the thickness of shell, *e*, can be calculated from the variation of the saturation magnetization, $M_{sat}$, with the reciprocal of the average diameter (1/*d*) of the particles according to equation suggested by Chen and co-workers[14]:

$$M_{sat} = M_{sat,bulk} \left(1 - \frac{6e}{d}\right) \qquad \text{(eq. S1)}$$
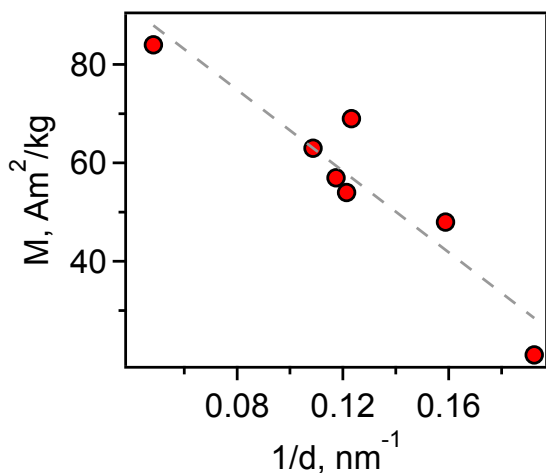


**Figure S8.** Saturation magnetization ($M_{sat}$) versus the reciprocal of the average diameter (1/*d*) of the prepared $Fe_3O_4$ nanoparticles.
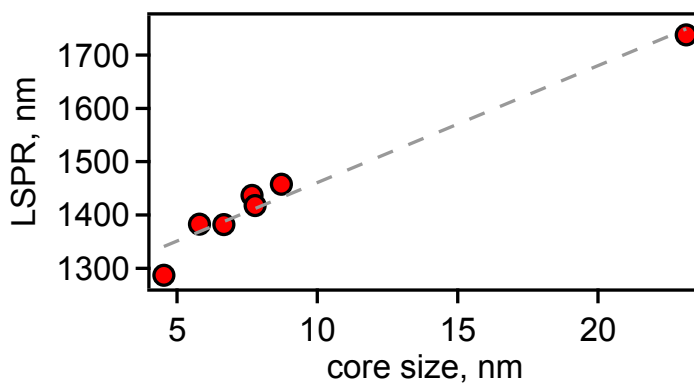


**Figure S9.** Core size versus LSPR maximum wavelength.

**Acid dissolution method.** Composition of $Fe_3O_4$ NCs ($Fe^{3+}/Fe^{2+}$ ratio) was determined using a combination of previously reported literature procedures.[15,16] The standard curve was established prior to the measurements using solutions with known $Fe^{2+}/Fe^{3+}$ ratios. Two solutions were prepared for each NC sample, one for detection of $Fe^{2+}$ and one for the detection of total iron in solution. To prepare the stock solution, 10 mg of $Fe_3O_4$ NCs was boiled in concentrated hydrochloric acid until all NCs were dissolved and no precipitation was detected upon cooling. Then, 10 μL of iron-containing solution was diluted with 800 μL of water and added to HOAc-NaAc buffer (1mL), 1,10-phenanthroline (400 μL, C = 5.5 mM), and hydroxylamine hydrochloride (400 μL, 1.6 M) mixture. The prepared solution was diluted with 100 μL of water or ascorbic acid solution (C = 5.8 M) to determine $Fe^{2+}$ or total iron, respectively. The absorbance of the above test solutions was measured at 510 nm, and the values of $Fe^{3+}$ and $Fe^{2+}$ were calculated using establish standard curve.
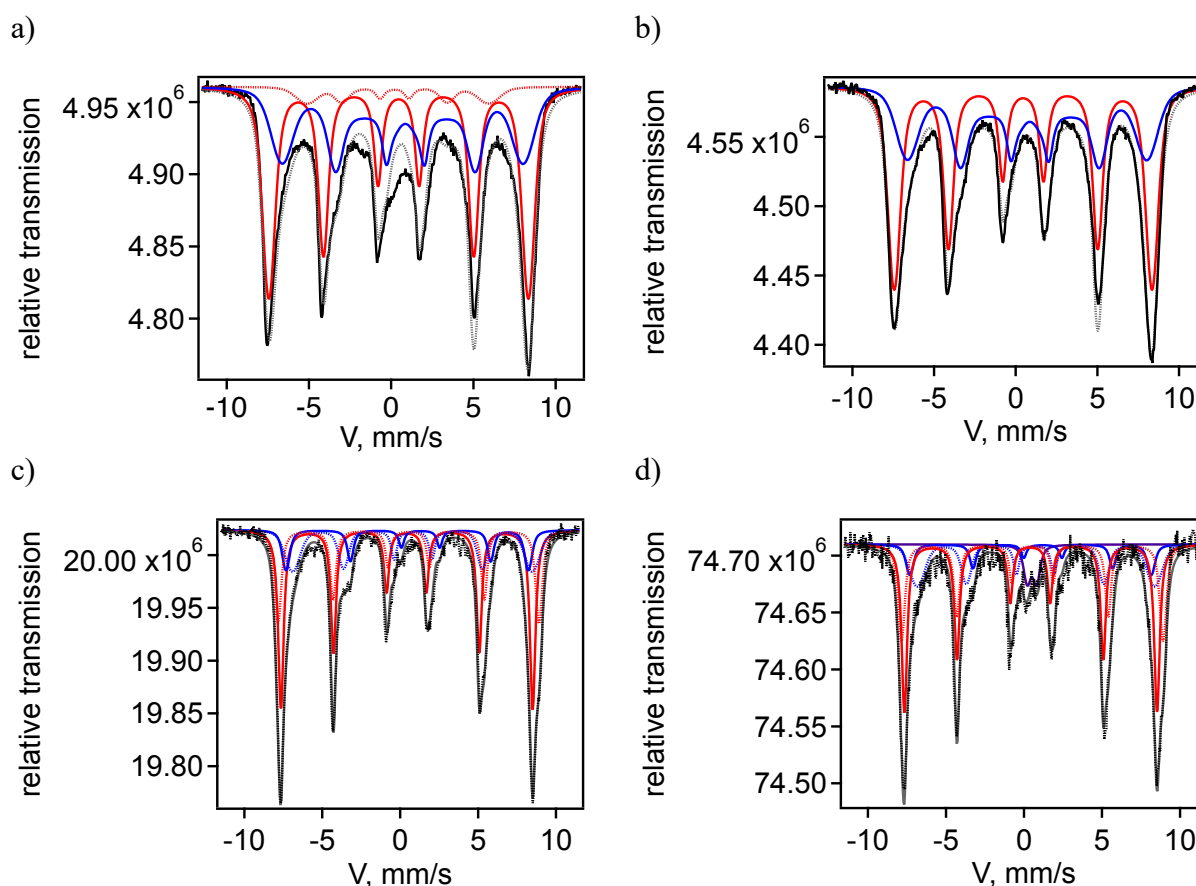


**Figure S10.** [57]Fe Mössbauer spectra of (a) **A-I-1**, (b) **A-I-2**, (c) **A-III-1**, and (d) **A-III-3**. Solid and dotted red lines represent components due to $Fe^{3+}$ ions in both tetrahedral and octahedral sublattices of inverse spinel. Blue lines are due to $Fe^{2.5+}$ (average of $Fe^{3+}$ and $Fe^{2+}$, couple involved in rapid exchange of electrons in the octahedral lattice). The nature of the small sextet in **A-I-1** is not certain.

**Table S2.** Composition data determined by $^{57}$Fe Mössbauer spectrometry and acidic dissolution method.

| Sample | $D_{TEM}$, nm | e, nm | $Fe^{2+}/Fe^{3+}$ | $Fe^{2+}/Fe^{3+}$ Based on shell % volume and 100% magnetite core | Magnetite core character | LSPR, nm |
|---|---|---|---|---|---|---|
| $^{57}$Fe Mossbauer spectrometry | | | | | | |
| A-I-1 | 5.2 | 0.67 | 0.29 | 0.20 | reduced | 1287 |
| A-I-2 | 6.3 | 0.50 | 0.29 | 0.30 | stoichiometric | 1383 |
| A-III-1 | 9.2 | 0.48 | 0.20 | 0.36 | oxidized | 1458 |
| A-III-3 | 8.2 | 0.56 | 0.18 | 0.32 | oxidized | 1437 |
| Acidic dissolution | | | | | | |
| A-III-1 | 9.2 | 0.48 | 0.27 | 0.36 | oxidized | 1458 |
| A-III-3 | 8.2 | 0.56 | 0.19 | 0.32 | oxidized | 1437 |
| A-II-4 | 20.7 | No magnetization data | 0.17 | | oxidized | 1693 |
| A-III-4 | 7.3 | 0.50 | 0.45 | 0.375 | reduced | 1382 |
| A-III-2 | 9.5 | No magnetization data | 0.11 | | | 1394 |

**Fabrication of coupled NP/QDs systems.** A saturated solution of iron nanoparticles in chloroform (150 µL) was diluted with 150 µL of chloroform and dispersed in 2 mL of hexane/octane mixture (9:1). The plasmonic thin films were prepared by spin-coating (200 rpm, 1 min, 3 times) of 50 µL of prepared suspension on quartz substrate followed by annealing at 300 °C for 5 min in an inert atmosphere. The separation distance between NPs and QDs was controlled by a nanoscale spacer layer. The thickness of the spacer layer was estimated by AFM. The layer of QDs was deposited on the top the already prepared $Fe_3O_4$/spacer thin films by drop casting 3 µL of QD suspension with known concentration.
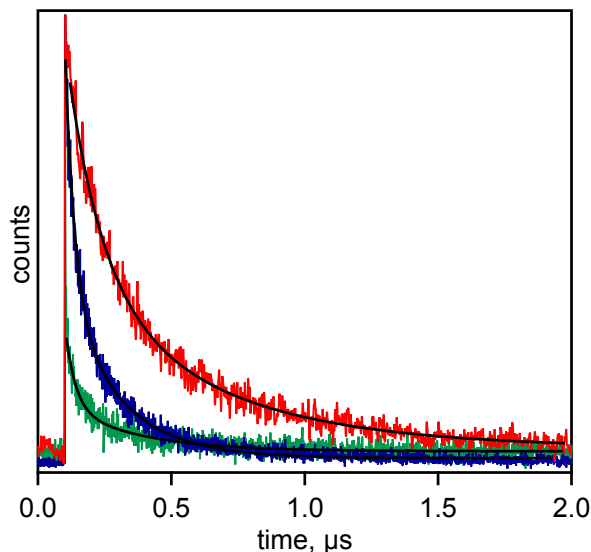


**Figure S11.** Fluorescence decays of QDs on PMMA film (red), $Fe_3O_4$ NCs thin films covered with PMMA spacer layer (blue), and $Fe_3O_4$ NCs thin film (green). Black solid lines are fits of decay.
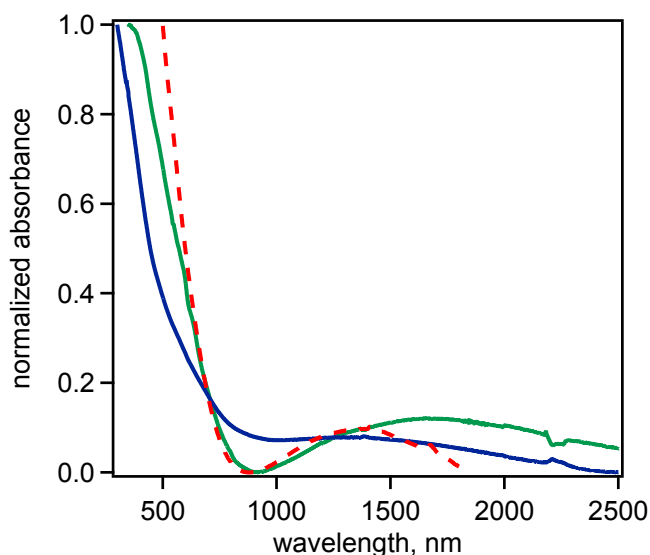


**Figure S12.** Normalized absorbance of $Fe_3O_4$ thin film covered with 10 nm layer of ChG spacer: GSS (blue) and GSST (green). Red dashed line corresponds to the normalized absorbance of corresponding $Fe_3O_4$ NPs dispersed in TCE.
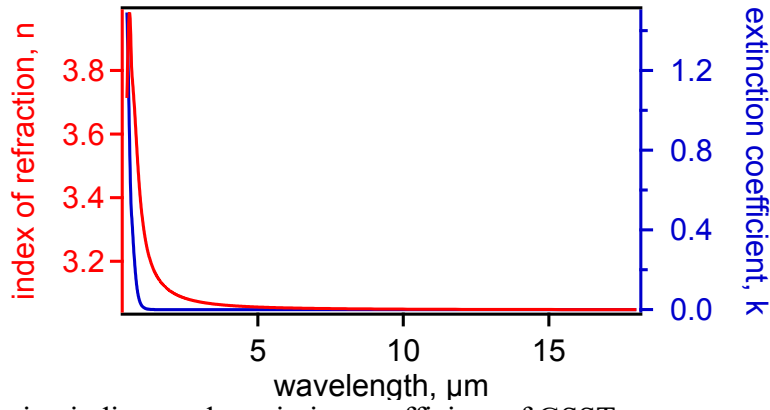
**Figure S13.** Refractive indices and exctintion coefficient of GSST spacer.
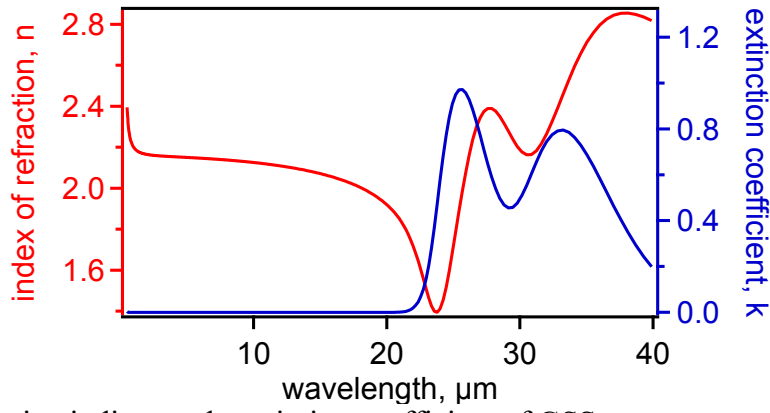


**Figure S14.** Refractive indices and exctintion coefficient of GSS spacer.

**Figure S15.** Fluorescence decays of QDs coupled to $Fe_3O_4$ NC thin film separated by spacer layer (a) GSS, (b) GSST and (c) $Al_2O_3$. Spacer thicknesses are 2.5 nm (dark blue), 5 nm (blue), 7.5 nm (green), 10 nm (yellow), 15 nm (orange), and 20 nm (red). (d) The Purcell factor as a function of spacer thickness for GSS (red), GSST (blue), and $Al_2O_3$ (gray) spacer materials.

The fluorescence decays were fit with biexponential function:

$$I(t) = \int_{-\infty}^{t} IRF(t) \sum_{i=1}^{n} B_i e^{[-\frac{t-t'}{\tau_i}]} dt'$$
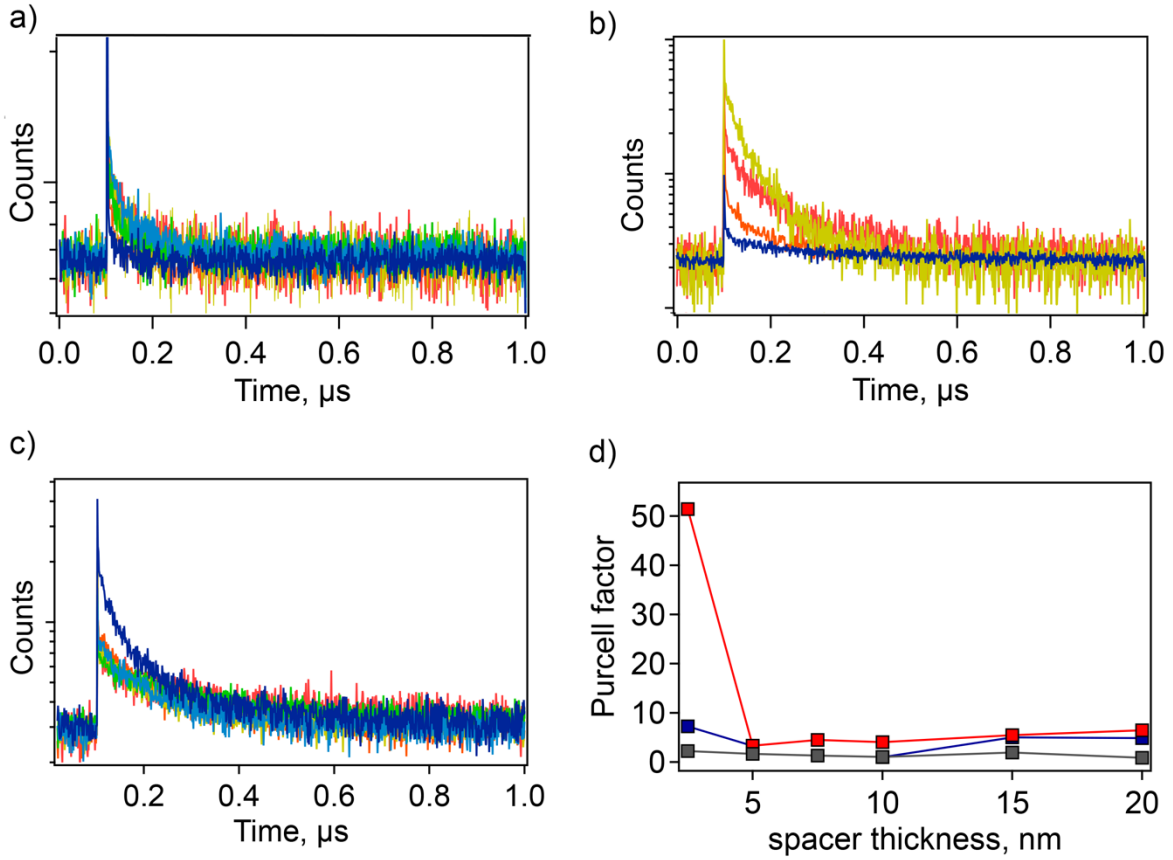
where $\tau$ and $B$ are lifetime and amplitude, respectively.

The amplitude-weighted average fluorescence lifetimes were calculated based on the following equation:

$$< \tau_{ave} > = \frac{B_1\tau_1 + B_2\tau_2}{B_1 + B_2}$$

Further analysis of *tr*-PL data shows that both decay constants, $\tau_1$ and $\tau_2$, extracted via bi-exponential fitting of decay curves (above), are affected by the presence of the NC layer. In general, both $\tau_1$ and $\tau_2$ are shorter in the presence of the NC layer in comparison with their respective control samples (i.e., in the absence of the plasmonic NC layer) (**Tables S3-S5**). At the same time, the contribution from the faster component, $\tau_1$, is significantly increased for the structures that showed the maximum spontaneous decay enhancement. According to previous work,[17] $\tau_1$ may be associated with emission from bi-exciton states, while $\tau_2$ may result from emissive decay of excitons. In this case, the relative enhancement of $\tau_1$ compared to $\tau_2$ could imply that bi-excitonic emission is preferentially enhanced compared to excitonic emission. However, additional studies are needed to confirm such a conclusion.

**Table S3.** GSS spacer

| Spacer thickness, nm | $B_1$ | $\tau_1$, ns | $B_2$ | $\tau_2$, ns | $<\tau_{ave}>$, ns |
|---|---|---|---|---|---|
| Control, without Fe$_3$O$_4$ NC layer | | | | | |
| 20 | 33.57 | 19.66 | 130.24 | 248.51 | 201.61 |
| 15 | 86.847 | 13.04 | 57.718 | 161.33 | 72.24 |
| 10 | 71.35 | 1.61 | 98.33 | 119.03 | 69.65 |
| 5 | 45.71 | 5.25 | 59.65 | 206.53 | 119.20 |
| 2.5 | 26.81 | 17.69 | 41.04 | 212.80 | 135.69 |
| With Fe$_3$O$_4$ NC layer | | | | | |
| 20 | 65.68 | 4.57 | 44.31 | 70.69 | 31.21 |
| 15 | 402.53 | 3.56 | 145.75 | 39.86 | 13.21 |
| 10 | 100.65 | 4.70 | 53.24 | 40.75 | 17.17 |
| 7.5 | 65.881 | 5.19 | 107.02 | 29.57 | 20.28 |
| 5 | 158.31 | 8.51 | 122.28 | 71.00 | 35.75 |
| 2.5 | 766.56 | 0.68 | 68.42 | 24.53 | 2.64 |

**Table S4.** GSST spacer

| Spacer thickness, nm | $B_1$ | $\tau_1$, ns | $B_2$ | $\tau_2$, ns | $<\tau_{ave}>$, ns |
|---|---|---|---|---|---|
| Control, without Fe$_3$O$_4$ NC layer | | | | | |
| 20 | 24.46 | 135.43 | 17.08 | 541.18 | 302.25 |

| | | | | | |
|---|---|---|---|---|---|
| 15 | 18.26 | 56.17 | 26.96 | 296.00 | 199.15 |
| 10 | 64.30 | 14.81 | 82.82 | 63.05 | 41.97 |
| 5 | 37.76 | 81.75 | 36.37 | 379.50 | 227.83 |
| 2.5 | 25.22 | 84.33 | 44.02 | 447.49 | 315.20 |
| With $Fe_3O_4$ NC layer | | | | | |
| 20 | 70.17 | 12.75 | 63.47 | 116.72 | 62.13 |
| 15 | 62.98 | 5.00 | 55.23 | 79.25 | 39.69 |
| 10 | 123.54 | 14.64 | 135.98 | 68.23 | 42.72 |
| 5 | 61.61 | 16.90 | 58.13 | 125.39 | 69.57 |
| 2.5 | 312.35 | 1.86 | 106.05 | 165.66 | 43.38 |

**Table S5.** $AlO_x$ spacer

| Spacer thickness, nm | $B_1$ | $\tau_1$, ns | $B_2$ | $\tau_2$, ns | $<\tau_{ave}>$, ns |
|---|---|---|---|---|---|
| Control, without QDs | | | | | |
| 20 | 41.17 | 79.95 | 34.662 | 226.77 | 147.06 |
| 15 | 24.319 | 42.95 | 57.889 | 285.70 | 213.89 |
| 10 | 48.60 | 50.24 | 71.68 | 167.62 | 120.19 |
| 7.5 | 45.644 | 85.99 | 38.003 | 391.74 | 224.90 |
| 5 | 75.025 | 60.51 | 74.297 | 245.48 | 152.54 |
| 2.5 | 95.148 | 42.92 | 101.05 | 186.33 | 116.78 |
| With QDs | | | | | |
| 20 | 33.894 | 23.32 | 38.595 | 295.04 | 167.99 |
| 15 | 85.515 | 41.78 | 122.82 | 158.73 | 110.73 |
| 10 | 74.83 | 48.64 | 97.39 | 165.98 | 115.00 |
| 7.5 | 39.36 | 17.57 | 101.26 | 228.87 | 169.72 |
| 5 | 53.87 | 16.30 | 110.86 | 129.19 | 92.27 |
| 2.5 | 187.73 | 13.74 | 163.89 | 96.54 | 52.33 |

**References:**

(1)     Krishnamurthy, S.; Singh, A.; Hu, Z.; Blake, A. V.; Kim, Y.; Singh, A.; Dolgopolova, E. A.; Williams, D. J.; Piryatinski, A.; Malko, A. V.; Htoon, H.; Sykora, M.; Hollingsworth, J.A. PbS/CdS Quantum Dot Room-Temperature Single-Emitter Spectroscopy Reaches the Telecom O and S Bands via an Engineered Stability. *ACS Nano* **2021**, *15*, 575–587.

(2)     Pool, V. L.; Klem, M. T.; Chorney, C. L.; Arenholz, E. A.; Idzerda, Y. U. Enhanced Magnetism of $Fe_3O_4$ Nanoparticles with Ga Doping. *J. Appl. Phys.* **2011**, *109*, 07B529.

(3)     Kim, D.; Lee, N.; Park, M.; Kim, B. H.; An, K.; Hyeon, T. Synthesis of Uniform Ferrimagnetic Magnetite Nanocubes. *J. Am. Chem. Soc.* **2009**, *131*, 454–455.

(4)     Urso, C.; Barawi, M.; Gaspari, R.; Sirigu, G.; Kriegel, I.; Zavelani-Rossi, M.; Scotognella, F.; Manca, M.; Prato, M.; De Trizio, L.; Manna, L. Colloidal Synthesis of Bipolar Off-Stoichiometric Gallium Iron Oxide Spinel-Type Nanocrystals with near-IR Plasmon Resonance. *J. Am. Chem. Soc.* **2017**, *139* (3), 1198–1206.

(5)     Chen, J.; Sorensen, C.; Klabunde, K. Size-Dependent Magnetic Properties o Fine Particles Synthesized by Coprecipitation. *Phys. Rev. B - Condens. Matter Mater. Phys.* **1996**, *54*, 9288–9296.

(6)     Rancourt, D. G.; Ping, J. Y. Voigt-Based Methods for Arbitrary-Shape Static Hyperfine Parameter Distributions in Mössbauer Spectroscopy. *Nucl. Instruments Methods Phys. Res. Sect. B Beam Interact. with Mater. Atoms* **1991**, *58*, 85–97

(7)     Boiteau, R. M.; Kukkadapu, R.; Cliff, J. B.; Smallwood, C. R.; Kovarik, L.; Wirth, M. G.; Engelhard, M. H.; Varga, T.; Dohnalkova, A.; Perea, D. E.; Wietsma, T.; Moran, J. J.; Hofmockel, K.S. Calcareous Organic Matter Coatings Sequester Siderophores in Alkaline Soils. *Sci. Total Environ.* **2020**, *724*, 138250.

(8)     Freysoldt, C.; Neugebauer, J.; Van de Walle, C. G. Electrostatic interactions between charged defects in supercells. *Phys. Stastus Solidi B* **2011**, *248*, 1067–1076.

(9)     Broberg, D.; Medasani, B.; Zimmermann, N. E. R.; Yu, G.; Canning, A.; Haranczyk, M.; Asta, M.; Hautier, G. PyCDT: A Python toolkit for modeling point defects in semiconductors and insulators. *Comput. Phys. Commun.* **2018**, *226*, 165–179.

(10)   Smiltens, J. The Standard Free Energy of Oxidation of Magnetite to Hematite at Temperatures above 1000°. *J. Am. Chem. Soc.* **1957**, *79*, 4877–4880.

(11)   Salmon, O. N. High temperature thermodynamics of the iron oxide system. *J. Phys. Chem.* **1961**, *65*, 550–556.

(12)   Basta, E. Z. Some mineralogical relationships in the system $Fe_2O_3$-$Fe_3O_4$ and the composition of titanomaghemite. *Econ. Geol.* **1959**, *54*, 698–719.

(13)   Ramdohr, P. The ore minerals and their intergrowth. Elsevier, **2013**.

(14)   Chen, J.; Sorensen, C.; Klabunde, K. Size-Dependent Magnetic Properties of Fine Particles Synthesized by Coprecipitation. *Phys. Rev. B - Condens. Matter Mater. Phys.* **1996**, *54*, 9288–9296.

(15)   Jiang, C.; Yang, S.; Gan, N.; Pan, H.; Liu, H. A Method for Determination of $[Fe^{3+}]/[Fe^{2+}]$ Ratio in Superparamagnetic Iron Oxide. *J. Magn. Magn. Mater.* **2017**, *439*, 126–134.

(16)   Tamura, H.; Goto, K.; Yotsuyanagi, T.; Nagayama, M. Spectrophotometric Determination of Iron(II) with 1,10-Phenanthroline in the Presence of Large Amounts of Iron(III). *Talanta* **1974**, *21*, 314–318.

(17)   Wang, F.; Karan, N. S.; Nguyen, H. M.; Ghosh, Y.; Sheehan, C. J.; Hollingsworth, J. A.; Htoon, H. Correlated Structural-Optical Study of Single Nanocrystals in a Gap-Bar Antenna: Effects of Plasmonics on Excitonic Recombination Pathways. *Nanoscale* **2015**, *7*,

9387–9393.